Acta Materialia 186 (2020) 40–49

Contents lists available at ScienceDirect

Acta Materialia

journal homepage: www.elsevier.com/locate/actamat

Full length article

Grain boundary properties of elemental metals

Hui Zheng[a,1], Xiang-Guo Li[a,1], Richard Tran[a], Chi Chen[a], Matthew Horton[b], Donald Winston[b], Kristin Aslaug Persson[b,c], Shyue Ping Ong[a,*]

[a] Department of NanoEngineering, University of California San Diego, 9500 Gilman Dr, Mail Code 0448, La Jolla, CA 92093-0448, United States
[b] Energy Technologies Area, Lawrence Berkeley National Laboratory, Berkeley, CA 94720, United States
[c] Department of Materials Science & Engineering, University of California Berkeley, Berkeley, CA 94720-1760, United States

ARTICLE INFO

Article history:
Received 26 July 2019
Revised 13 December 2019
Accepted 14 December 2019
Available online 19 December 2019

Keywords:
Grain boundary
DFT
Database
Predictive modeling

ABSTRACT

The structure and energy of grain boundaries (GBs) are essential for predicting the properties of polycrystalline materials. In this work, we use high-throughput density functional theory calculations workflow to construct the Grain Boundary Database (GBDB), the largest database of DFT-computed grain boundary properties to date. The database currently encompasses 327 GBs of 58 elemental metals, including 10 common twist or symmetric tilt GBs for body-centered cubic (bcc) and face-centered cubic (fcc) systems and the Σ7 [0001] twist GB for hexagonal close-packed (hcp) systems. In particular, we demonstrate a novel scaled-structural template approach for HT GB calculations, which reduces the computational cost of converging GB structures by a factor of ~ 3–6. The grain boundary energies and work of separation are rigorously validated against previous experimental and computational data. Using this large GB dataset, we develop an improved predictive model for the GB energy of different elements based on the cohesive energy and shear modulus. The open GBDB represents a significant step forward in the availability of first principles GB properties, which we believe would help guide the future design of polycrystalline materials.

1. Introduction

The majority of engineering materials are polycrystals, comprising a large number of grains whose interfaces form grain boundaries (GBs). The GB character distribution (GBCD) [1], i.e., the type and frequency of GBs present, strongly affects a material's mechanical properties [2,3] such as hardness [4], brittleness [5,6], creep-strength [7], corrosion resistance [8], fatigue strength [9], and weldability [10]. For instance, intergranular fracture is the primary origin of severe brittleness and fatigue failure, and GBs are the preferential sites for the nucleation and propagation of fatigue cracks [5,11]. Manipulating the GBCD through various processing techniques is a common pathway to improving the mechanical properties of structural metals and alloys [3,5,9,12,13].

The GBCD of a material is related to the relative GB formation energies [14]. In thermodynamic equilibrium, the lower the formation energy for a particular type of GB (otherwise simply known as the GB energy or γ_{GB}), the greater its prevalence in the polycrystal [5,14,15]. A variety of experimental techniques (e.g., thermal groove, orientation imaging microscopy) have been applied to investigate γ_{GB}, but the data sets were limited due to the difficulty of measuring accurate γ_{GB} [16–22]. Recently Rohrer et al. have developed a high-throughput (HT) experimental method to measure γ_{GB} for large ensembles of GBs by inversely correlating it with the statistical abundance of GB types present in the polycrystal [14,23,24]. This method has been applied to fcc Ni [25], Ni-based alloys [14], W thin film [26], ferrite (mainly bcc Fe) [27], austenitic steel (mainly fcc Fe) [28] and hcp Ti [29]. Such HT studies have significantly increased the available experimental data for γ_{GB} [15,25]. However, this statistical approach suffers from a strong dependence of the uncertainty in the measured γ_{GB} on the frequency of observed GBs, leading to unreliable measurements for GBs of lower frequency. Furthermore, the method yields relative, rather than absolute, γ_{GB}.

Computationally, there have been many investigations of γ_{GB} using both empirical and first principles methods. Studies using empirical interatomic potentials (IAPs) such as the embedded atom method (EAM) [30–32] and Lennard–Jones [30,31] potentials are typically limited to a few elemental systems belonging to a specific crystal prototype (e.g., fcc or bcc), but cover a broad range of GB types [33–38]. The reason is because the fitting of sufficiently accurate IAPs is a relatively complex and resource-intensive process, but once fitted, it is inexpensive to use the IAP to compute many

* Corresponding author.
E-mail addresses: ongsp@eng.ucsd.edu, s2ong@ucsd.edu (S.P. Ong).
[1] These authors contributed equally.

https://doi.org/10.1016/j.actamat.2019.12.030
1359-6454/

GB structures comprising thousands or even millions of atoms. For instance, Olmsted et al. [35], Holm et al. [36,39] have calculated γ_{GB} for 388 distinct GBs of fcc Ni, Al, Au, and Cu using EAM and found that GB energies in different elements are strongly correlated. For bcc metals, Ratanaphan et al. [38] have computed the energies of 408 distinct GBs in bcc Fe and Mo ranging from Σ3 to Σ323. Their results show that GB energies are influenced more by GB plane orientation than by lattice misorientation or lattice coincidence.

With computing advances, calculations of γ_{GB} using accurate, but expensive first-principles methods such as density functional theory (DFT) have become increasingly common. In contrast to IAP-based studies, DFT studies tend to be broader in chemical scope but narrow in the range of GB structures studied (typically limited to low Σ GB models of hundreds of atoms). This is due to the universal applicability, but high computational expense, of DFT methods. For example, Scheiber et al. [40] have computed 14 types of GBs for W, Mo and Fe using DFT, while Wang et al. [41] have calculated 11 types of low sigma ($\Sigma < 13$) symmetrical tilt GBs and 2 twist GBs for bcc Fe. Bean and McKenna [42] have also used DFT calculations to verify a small subset of symmetric tilt GB structures acquired from EAM calculations in Cu and Ni systems.

In this work, we report the development of the Grain Boundary DataBase (GBDB), a comprehensive database for GB properties (γ_{GB}, work of separation W_{sep}) for a broad range of low-index GB structures (tilt and twist) for fcc, bcc, and hcp elemental metals using high-throughput DFT calculations. At the time of writing, this GBDB contains data on 327 GB structures for 58 elements, with more GB types and elements continually being added. This GBDB has been made available via the Materials Project and its Application Programming Interface [43,44], together with a user-friendly web application called Crystal Toolkit for the generation of GB structures. A critical enabler to the construction of the GBDB is an innovative lattice scaling approach, which substantially lowers the computational effort in performing GB calculations for similar crystal types across different elements. Finally, we rigorously validate the GBDB against prior experimental and computed data, and using this large dataset, develop an efficient model for predicting γ_{GB} for different elements.

2. Methods

2.1. Grain boundary model generation

Fig. 1 shows the schematic of the GB model generation algorithm, which is based on the coincident-site lattice (CSL) method [45]. For two grains misoriented by a rotation angle about a rotation axis, the superposition of the two crystals result in coincident sites forming a sublattice of the two crystal lattices, i.e., a CSL. An important parameter characterizing the CSL is the Σ value, defined as the ratio of the unit cell volume of the CSL to the volume of the generating bulk cell. A GB can be completely and unambiguously described by five macroscopic degrees of freedom (DOFs) [46], e.g. Σ5 36.87°/[100](031). Three DOFs describe the mutual misorientations between two adjoining grains, two of which define the rotation axis (two DOFs, e.g. [100]) and one of which defines the rotation angle, e.g. 36.87°. The remaining two DOFs describe the GB plane, e.g. (031). In addition to these five independent macroscopic DOFs, three microscopic DOFs characterise a rigid body translation of two grains relative to each other [46]. The steps in the algorithm are as follows:

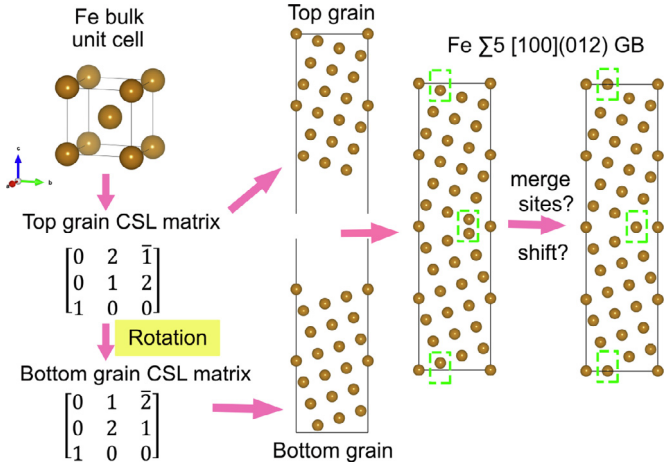

Fig. 1. Grain boundary generation process.

- Starting from the unit cell (primitive or conventional cell) with lattice type of cubic, tetragonal, orthorhombic, hexagonal or rhombohedral, a series of lattice vector transformations is performed to create an unit cell of CSL with the a and b lattice vectors parallel to the input GB plane.
- Two grains are created and rotated relative to each other based on the inputs (rotation axis and angle, expansion times of the CSL unit cell along *c* direction).
- The two grains are then stacked to form the periodic GB structure. The relative shifts between the two grains along the *a, b* and *c* directions can be adjusted.
- Finally, sites that are too close to each other based on a distance tolerance set by the user are merged.

The above algorithm is implemented in the open-source Python Materials Genomics (pymatgen) materials analysis library [43], together with methods for finding all sigma values and their corresponding rotation angles for any given input structure and rotation axis. A user-friendly graphical user interface to the algorithm is also available on Materials Project website Crystal Toolkit application (https://materialsproject.org/#apps/xtaltoolkit).

2.2. GB property computation

The GB energy (γ_{GB}) is defined by the following expression:

$$\gamma_{GB} = \frac{E_{GB} - n_{GB}E_{bulk}}{2A_{GB}} \quad (1)$$

where E_{GB} and n_{GB} are the total energy and number of atoms of the GB structure, respectively, A_{GB} is the cross-sectional area of the GB, E_{bulk} is the energy per atom of the bulk, and the factor of 2 in the denominator accounts for the two grain boundaries in the GB model.

Another GB property of interest is the work of separation W_{sep}, which is a measure of the energy required to cleave the GB into the free surfaces and is correlated to the fracture toughness [47–50]. W_{sep} is given by the following expression:

$$W_{sep} = 2\gamma_{surf} - \gamma_{GB} \quad (2)$$

where γ_{surf} is the corresponding surface energy for the facet (*hkl*) formed by cleaving the GB. Previously, some of the current authors have already constructed a comprehensive database of the surface energies of the elements [51], which are used in this work in the computation of W_{sep}.

2.3. DFT computations

All DFT energy calculations were performed using the Vienna Ab initio Simulation Package (VASP) [52] with the projector augmented wave (PAW) [53,54] method. The exchange-correlation effects were modeled using the Perdew-Berke-Ernzerhof (PBE)

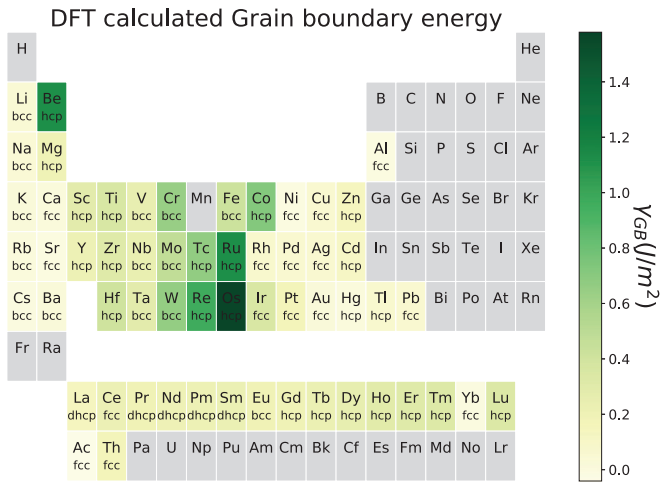

Fig. 2. DFT calculated GB energy. For bcc and fcc, the lowest γ_{GB} types, i.e., Σ3[110](112) for bcc and Σ3[111](111) for fcc are plotted. For hcp, and double-hcp (dhcp) elements, Σ7(0001) GBs are chosen to be represented in this periodic table heatmap.

Table 1
GB types calculated in this work. Note: The Σ7[111](111) twist GBs of bcc Li, Na, K, Rb, Cs and Ba have 336 atoms instead of 168.

Sigma	type	R-axis	R-angle	GB-plane	Join-plane	No. of atoms	
						bcc	fcc
3	tilt	[110]	109.47	(1 $\bar{1}$ $\bar{2}$)	($\bar{1}$ 1 $\bar{2}$)	24	46
3	tilt	[111]	180	(1 $\bar{1}$ 0)	(0 1 $\bar{1}$)	48	56
3	twist	[111]	60	(1 1 1)	(1 1 1)	48	24
5	tilt	[100]	36.87	(0 $\bar{1}$ $\bar{2}$)	(0 2 1)	38	38
5	tilt	[100]	53.13	(0 $\bar{1}$ $\bar{3}$)	(0 3 1)	40	58
5	twist	[100]	36.87	(1 0 0)	(1 0 0)	80	80
7	twist	[111]	38.21	(1 1 1)	(1 1 1)	168*	84
7	tilt	[111]	38.21	(1 $\bar{3}$ 2)	($\bar{2}$ 3 $\bar{1}$)	54	54
9	twist	[110]	38.94	(1 1 0)	(1 1 0)	126	180
9	tilt	[110]	38.94	(2 $\bar{2}$ 1)	(2 $\bar{2}$ 1)	70	70
						hcp/dhcp	
7	twist	[0001]	21.79	(0 0 0 1)	(0 0 0 1)	112	

[55] generalized gradient approximation (GGA) functional. The plane wave energy cutoff is 400 eV. The *k*-point grid for structure relaxation is 30 per Å^{-1} in *a* and *b* directions (GB plane), and a denser grid of 45 per Å^{-1} is applied for single-point energy calculations. The energies and atomic forces of all calculations were converged within 10^{-4} eV and 0.02 eV Å^{-1} (see Table S1 for force convergence tests on Mo). Through a series of convergence tests (see Fig. S3), it was determined that a minimum normal distance of ~ 25 Å between periodic boundaries (2 × the distance between GBs) is sufficient to minimize interactions between the two grain boundaries, such that γ_{GB} is converged to within 0.05 J m^{-2}. It should be noted that this 25Å refers to the minimum distance, and the average distance between periodic boundaries is ~ 40 Å (see Fig. S4).

2.4. Scope and availability of data

Our database covers a total of 58 elements (see Fig. 2), with 10 GB types for fcc and bcc and one GB type for hcp and double-hcp (dhcp) elements (see Table 1), with a total of 327 GB structures. We limit the GB types in this study with the following criteria:

1. Σ < 10
2. Maximum Miller index (MMI) of rotation axis ≤ 1
3. MMI of GB plane ≤ 3.
4. All tilt GBs are symmetric.

All GB structures and properties are available on the Materials Project (https://materialsproject.org/) [43,44] and Crystalium (http://crystalium.materialsvirtuallab.org) [51] websites. A visual inspection of all 327 GB structures revealed no abnormal structures.

3. Results

3.1. Benchmarking

A major bottleneck to calculations of GBs is that the large system sizes combined with difficult convergence of atomic positions, especially close to the GB region, render such computations relatively expensive compared to bulk crystal calculations. Furthermore, in order to obtain the global minimum configuration, it is necessary to perform a complete grid search over translations of the grains in all three crystallographic directions. However, such an effort would be prohibitively expensive for a high-throughput database construction. To accelerate such computations, we designed a scheme to find reasonable low-energy (not necessarily the global lowest) GB configurations. A fundamental hypothesis explored in this work is that similar crystal structures (e.g., bcc, fcc, or hcp) tend to lead to similar low-energy GB configurations, and an efficient step-wise translation search scheme was used as opposed to a full grid search to identify low-energy GB configurations.

The efficient search scheme proceeds by applying rigid body translation [37] of two grains to each type GBs and performing a static calculation for each translation vector. The search was performed in two steps. First, a search was performed for the optimal inter-grain separation by translating the two grains along the ***c*** direction in increments of 10% of the lattice parameter of the conventional unit cell. In the second step, a grid search for the optimal ***a*** and ***b*** translations in increments of 5%–12.5% of the basal lattice vectors (***a*** and ***b***) was performed using the optimal ***c*** translation from the first step. The results (see Figs. S1 and S2) show that basal plane translations contribute to an energy difference of < 0.05 J m^{-2} for most GBs of Mo and Nb, with the largest energy difference of 0.125 J m^{-2} for Σ5(013) twist GB of Mo (see Tables S2). As such, for the purposes of the high-throughput GB data generation, the GBs were generated with no basal plane translations. We also note that a full grid search in all three crystallographic directions using 12 GBs of Nb and Mo reached similar conclusions, justifying the use of the step-wise search (see Table S3). For symmetric tilt GBs, atoms at the interface that are less than 70% of the bulk interatomic distance apart are merged.

Based on these results, we have developed a high-throughput workflow for GB calculations using the Atomate software package [43,56,57], as shown in Fig. 3. For each structural prototype (bcc, fcc, hcp and dhcp), we first compute a series of fully-relaxed GB templates for all the GB types investigated in this work (see Table 1), using Mo, Cu and Be/La as the templates for bcc, fcc and hcp/dhcp structures, respectively. Initial structures for GB computations of each element M are then created from these GB templates by applying a scaling factor of $\frac{a_M}{a_{prototype}}$ to the template GB lattice constants for all materials, where a_M and $a_{prototype}$ are the bulk lattice parameters of the metal M and prototype element respectively. No scaling is applied for Zn and Cd, which are hcp elements with anomalous c/a ratios (1.986 and 1.915, respectively, from our PBE calculations, which is consistent with previous DFT studies [58]) that deviate substantially from the ideal ratio of 1.633, and their GB structures were generated directly from the bulk structure. A full relaxation is then performed on the scaled GBs. The use of the scaled GB templates significantly reduces the computational resources for the most time-consuming structural relaxation step by a factor of ~ 3–6, with higher speed-ups for

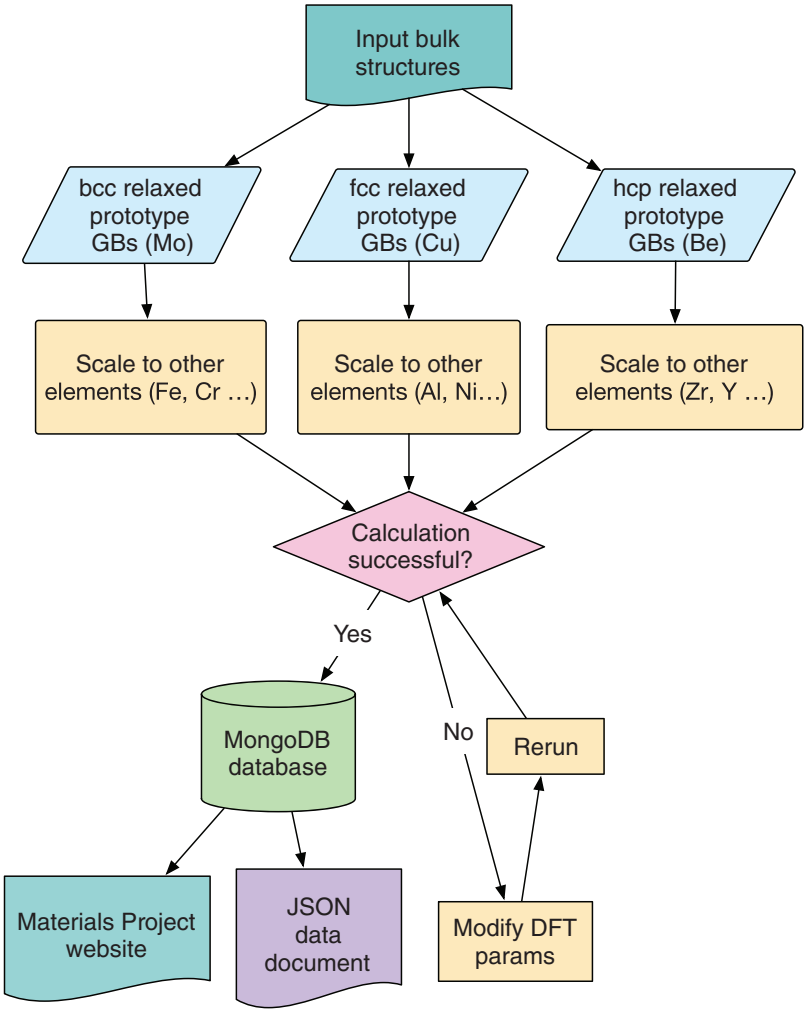

Fig. 3. High-throughput computational workflow for elemental grain boundaries.

Table 2
CPU hours for GB relaxation with and without the use of scaled prototype templates.

Element	GB type	# of atoms	CPU hours		
			No template	With template	Speed up
bcc-Ba	Σ3(111)	48	2560.00	716.80	3.57
bcc-Fe	Σ9(110)	126	2340.00	508.33	4.60
fcc-Sr	Σ5(100)	80	2128.05	344.29	6.18
fcc-Ag	Σ5(013)	80	97.67	97.55	1.00
hcp-Ti	Σ7(0001)	112	24.28	13.94	1.74
dhcp-Nd	Σ7(0001)	112	218.39	59.08	3.70

GBs with larger number of atoms and GBs that are very different from bulk (Table 2). More accurate static calculations with denser *k*-point meshes were then performed to obtain the final total energy of the GB structures. The results were then automatically inserted into a MongoDB document-based database.

We believe our step-wise search scheme combined with the GB template strategy provides a highly efficient approach to generating low-energy GB configurations with energies that are reasonably close to the global minimum. Furthermore, the database can be readily updated to incorporate new lower energy GB configurations as they are reported.

3.2. Grain boundary energies

Fig. 4 shows the distribution of γ_{GB} for bcc, fcc, and hcp elements. All values are tabulated in Tables S4 and S5 for reference. For bcc elements (Fig. 4(a)), we can observe a substantial jump in γ_{GB} from alkali/alkaline earth metals to transition metals; the γ_{GB} for alkali and alkaline earth metals are less than 0.3 Jm^{-2}, while those for the transition metals are at least four times higher. γ_{GB} for fcc elements follows a similar trend but with a more gradual increase (see Fig. 4(b)). Group VIII elements have high γ_{GB} while group IB, IIA, and IIB elements have relatively low γ_{GB}. Fig. 4(c) shows the γ_{GB} distribution for hcp/dhcp Σ7(0001) grain boundaries. For transition metals, we observe that γ_{GB} peaks at groups VIIB and VIII (Tc, Co, Re, Ru, and Os). All the rare earth and group IIA elements have lower GB energies than the transition metals with the exception of Be, which has a much higher GB energy. The rare earth elements show a gradual increase in γ_{GB} as group number increases.

The γ_{GB} distribution across different GB types varies with the crystal type. The two coherent twin boundaries, Σ3(111) for fcc and Σ3(112) for bcc, have the lowest γ_{GB} within the respective crystal prototypes. GBs terminated by the most atomically-dense planes ((111) for fcc and (110) for bcc) have lower γ_{GB} than other planes in general. Consequently, the fcc Σ7(111) and bcc Σ3(011) GBs correspond to the second lowest γ_{GB} for fcc and bcc,

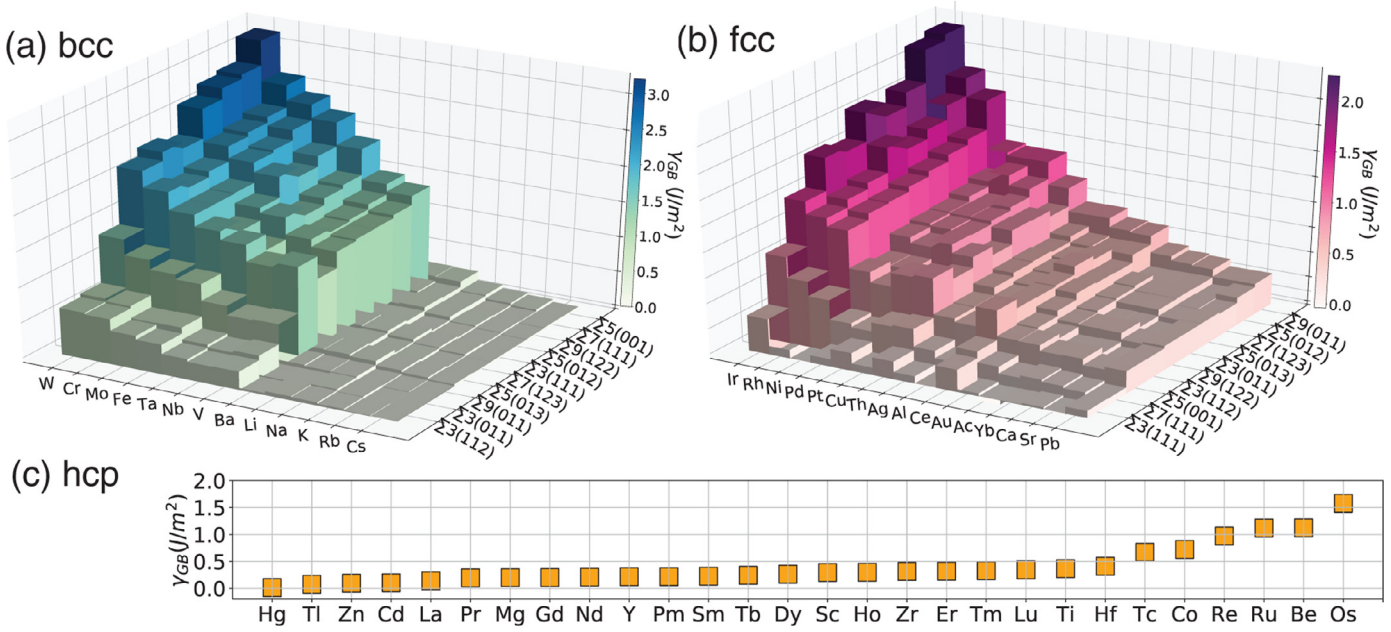

Fig. 4. GB energy γ_{GB} distribution for (a) bcc, (b) fcc, and (c) hcp/dhcp elemental metals, sorted by increasing γ_{GB}.

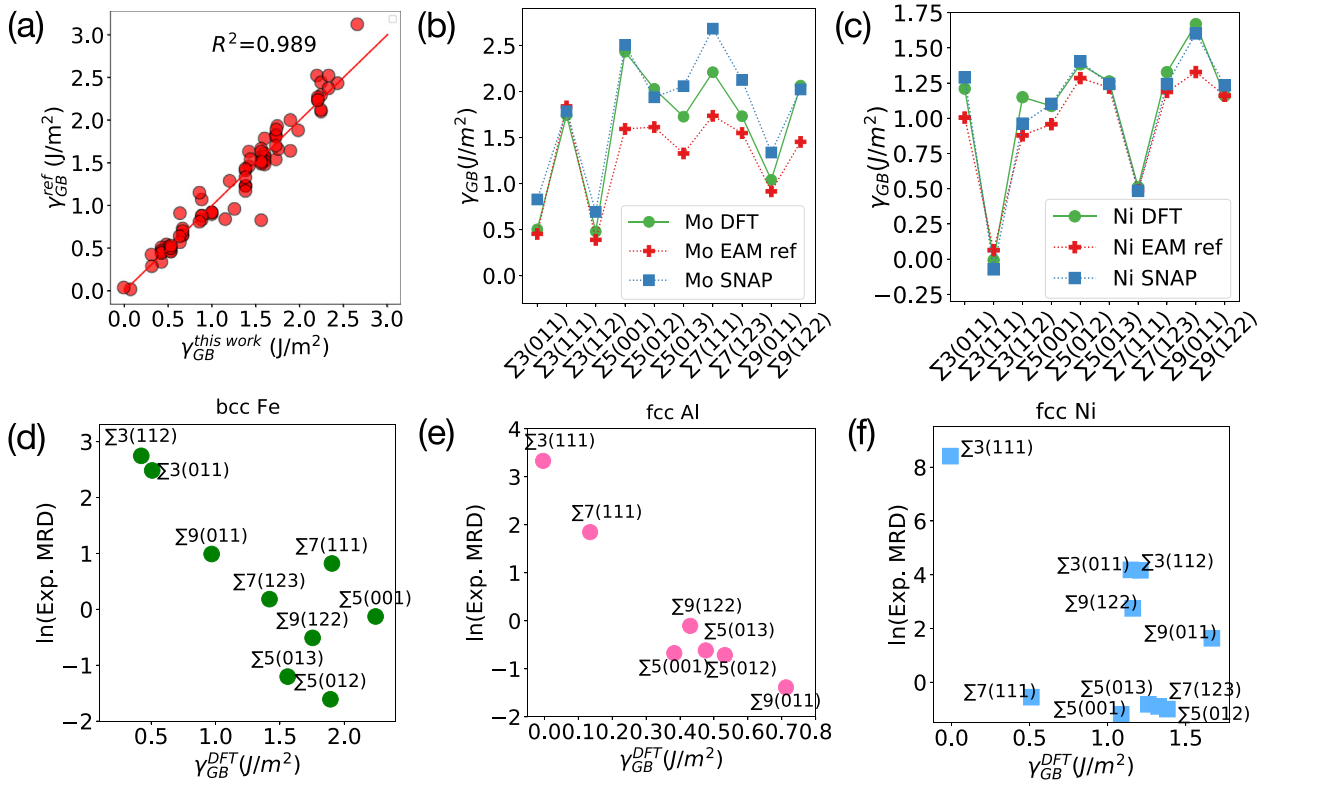

Fig. 5. Comparison of γ_{GB} between this work and (a) previous DFT values; (b) and, (c) EAM [35,38] and SNAP [99,100] values. (d), (e) and (f) compare our the calculated γ_{GB} of bcc Fe, fcc Al, and fcc Ni with experimentally measured MRD [25,60,61].

respectively. This is in agreement with both previous atomistic calculations [31,32,36,38,59] and experimental results [15,26,39,60]. For example, it has been observed experimentally that the most frequently observed GB for fcc Ni and Al is the Σ3(111) twin boundary, and other GBs terminated with the (111) plane also have a high population [25,60]. For bcc metals, our data shows that the Σ3(112) symmetric tilt GB (twin) has the lowest energy, which agrees with experiments performed in bcc W thin films [26] with nanoscale grain sizes and bcc ferritic/interstitial free steel [27,61]. It should be noted that a few GBs have unphysical negative γ_{GB} values that are very close to zero ($<$ 0.02 Jm^{-2}). These can be attributed to small numerical convergence errors. Most of these GBs are coherent twin boundaries of fcc Sr, Ni, and Al, which are well-known to have extremely small GB energies. [25]

Fig. 5 shows the validation of our computed γ_{GB} with previous DFT calculations [40–42,62–97], atomistic calculations [98] us-

ing machine-learned spectral neighbor analysis potentials (SNAP) [99,100] and the embedded atom method (EAM) [35,38,39], and experimental data [15,25,26,61]. From Fig. 5(a) and Table S8, we may observe that the most frequently studied systems are Fe [40,41,62–66,80–83,90,101–105], Al [68–73], Cu [42,75–79,106–108], Mo [40,67,84–86,109], W [40,67,94–96,109,110] and Ni [42,66,80,87–89,91,92] due to their important applications in steel, automobile, and aerospace industries. The high computational cost of DFT methods and the lack of efficient GB generation tool limit the previous studies to mostly low sigma symmetric tilt GBs, such as Σ5[100](012) [41,42,63,69–76,80,87–89,91,92,96], Σ5[100](013) [40,41,64–67,75,77–79,83–86,90,96,106], Σ3[110](111) [40–42,62–64,74,80–82,93,95,96], Σ3[110](112) [40–42,64,65,68,75,83,94–96], etc. Our GBDB includes both these popular GB types and some other twist GB types for 58 elemental systems. When comparing to these GB data available in previous DFT work, our computed γ_{GB} have an excellent agreement, with a R^2 close to unity and a very small standard error of 0.013 J/m^2.

Similarly, we find good agreement between the calculated γ_{GB} for different GBs of Mo and Ni with those computed using the state-of-the-art SNAP models [99,100], while the EAM predicted GB energies [35,38] are substantially underestimated as shown in Fig. 5(b) and (c). For bcc Mo, values of γ_{GB} using SNAP are slightly larger than most DFT values with the exception of the Σ5(012) GB where SNAP slightly underestimates DFT values. For fcc Ni, the γ_{GB} values of both EAM and SNAP are consistent with our DFT values, further supporting the conclusion that EAM performs better in fcc systems than bcc systems [100].

Fig. 5(d), (e) and (f) plot the natural log of the experimentally measured multiples of random distribution (MRD), i.e. the experimental average population of GBs, against the DFT calculated GB energy (γ_{GB}^{DFT}) for Fe, Al and Ni, respectively. We observe a negative correlation between the ln(*MRD*) and γ_{GB} similar to that reported previously for Ni [25].

3.3. Work of separation

The thermodynamic threshold energy for GB fracture, or work of separation (W_{sep}), can be defined as the difference between the surface energy and GB energy as shown in Eq. (2). Since the formation of surfaces and GBs both relate to bond breaking and distortion, we expect GB energy γ_{GB}, surface energy γ_{surf} and work of separation W_{sep} to be positively correlated with cohesive energy. This is demonstrated in Fig. 6 for bcc Σ3(110), fcc Σ3(111) and hcp Σ7(0001) GBs. The values of W_{sep} for all other GB types are provided in Table S6 and S7. This positive correlation is in agreement with previous bond breaking arguments [33,34]. The variation trend of W_{sep} is mainly dominated by γ_{surf} due to the small value of γ_{GB}. In general, the variation in anisotropic surface energies across different surfaces is smaller compared to the GB energy variation across different types of GBs as shown in Fig. S5. As such, we can expect a negative correlation between GB energy and work of separation as shown in Figs. S6 and S7.

Fig. 7 plots the experimentally measured ultimate tensile strength (UTS) [111] against the calculated W_{sep} for the GB with lowest γ_{GB}, i.e., the likely dominant GB type. A general positive relationship is observed between W_{sep} and UTS, as expected. The non-monotonic relationship may be due to the different processing methods (e.g., annealing, heat treatment, cold-worked) that can significantly affect micro-structure, and hence measured UTS.

3.4. Multiple linear regression model for γ_{GB}

Using the extensive set of computed γ_{GB}, we have developed a multiple linear regression (MLR) model for γ_{GB} for each GB type

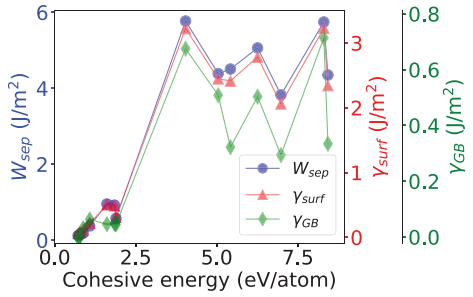

(a) bcc Σ3(110)

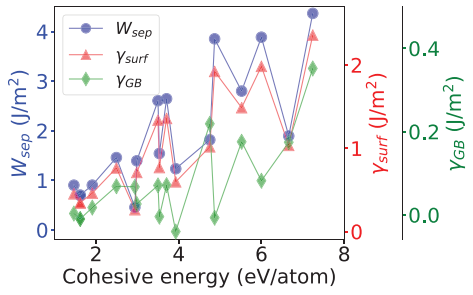

(b) fcc Σ3(111)

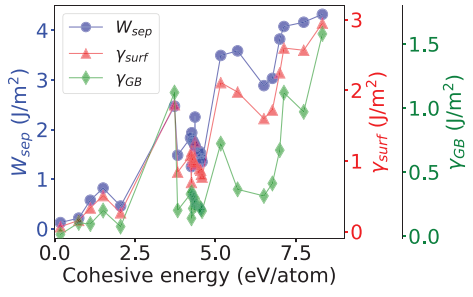

(c) hcp Σ7(0001)

Fig. 6. Comparison between surface energy (γ_{surf}), GB energy (γ_{GB}) and work of separation (W_{sep}) for (a) bcc Σ3(110), (b) fcc Σ3(111) and (c) hcp Σ7(0001) GBs, plotted in order of ascending cohesive energy E_{coh} of the element. While all three quantities show a general positive trend with the cohesive energy, the range of W_{sep} is much larger than γ_{surf}, which are in turn much larger than γ_{GB}.

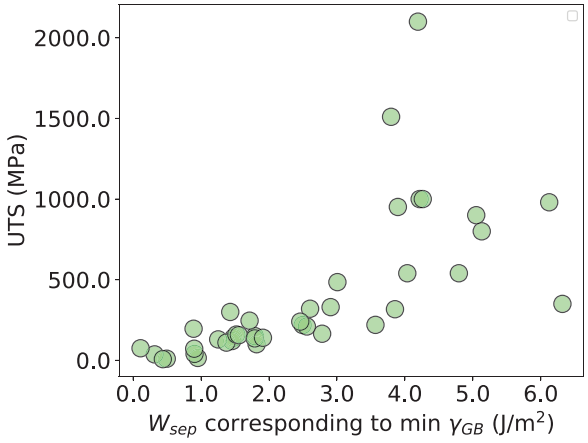

Fig. 7. Relationship between calculated work of separation W_{sep} for GB with lowest γ_{GB} and experimentally measured ultimate tensile strength (UTS) [111].

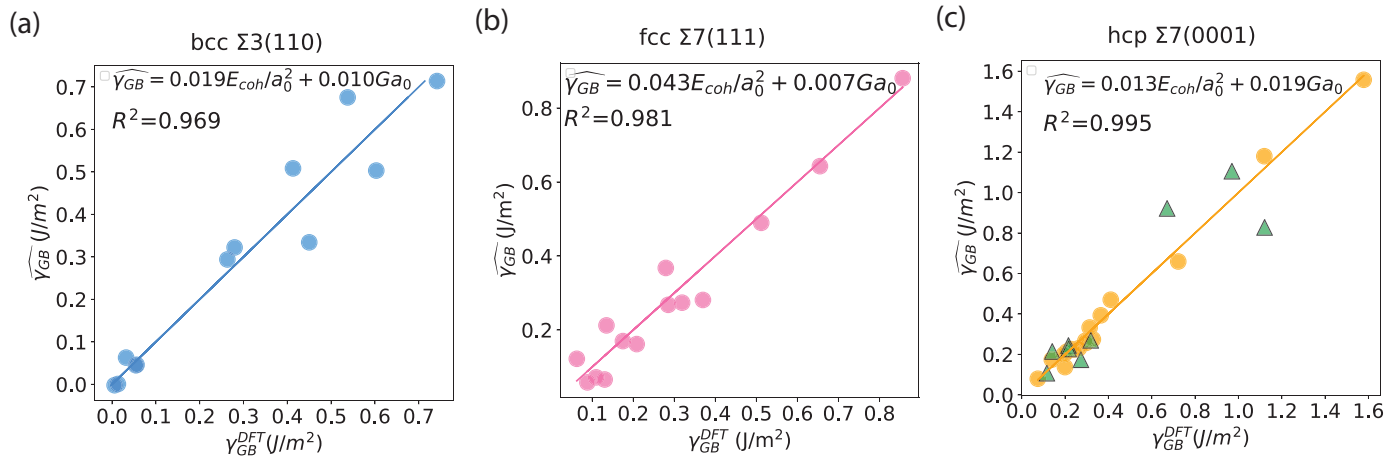

Fig. 8. Multiple linear regression models for the (a) bcc Σ3(110), (b) fcc Σ7(111), and (c) hcp Σ7(0001) GBs.

by fitting to the following equation:

$$\widehat{\gamma_{GB}} = \beta_1 E_{coh} a_0^{-2} + \beta_2 G \cdot a_0 \tag{3}$$

where $\widehat{\gamma_{GB}}$ is the fitted GB energy, E_{coh} is the cohesive energy, a_0 is the lattice parameter of corresponding conventional bulk cell (Å), and G is the Voigt–Reuss–Hill shear modulus (Jm^{-3}) [112,113]. This model choice is an amalgamation of models proposed in previous works. Ratanaphan et al. have found that the γ_{GB} of bcc Fe and Mo are strongly correlated with the cohesive energy (E_{coh}) [38]. Previous EAM-based GB databases have also found that γ_{GB} for fcc metals such as Al, Au, Cu and Ni are strongly correlated to the c_{44} elastic constant [35,36]. Furthermore, the Read–Shockley dislocation model [114] treats GBs with small misorientation angles as an array of dislocations whose energy is proportional to a shear modulus. In essence, the $E_{coh}a_0^{-2}$ term in Eq. (3) accounts for the contribution of broken bonds to γ_{GB}, while the $G \cdot a_0$ term accounts for the contributions from distorted (stretched, compressed) bonds. Both terms have been scaled by powers of the lattice constant such that the coefficients β_1 and β_2 are dimensionless.

Fig. 8 shows the fitting results for three GB types (see Figs. S8 and S9 for the remaining GB types). In general, the MLR models exhibit good predictive accuracy across all GB types, with $R^2 > 0.9$. We note that each GB type has different fitted values of the dimensionless coefficients β_1 and β_2 due to different contributions from bond breaking and bond distortion. We provide an example to show the predictive ability of our linear regression model. In Fig. 8(c), the orange circles are the data points used to build the MLR model, and the green triangles are a "test set" of elemental GBs. It can be seen that the performance on the "test set" is similar to that of the training set. We show that these results hold for all the GB structures computed in this work, and we believe it will hold for GB structures of larger Σ values for which the model GB structure can contain many more atoms and hence are more expensive to compute. The implication of these results is that a predictive MLR model can potentially be constructed using a smaller set of elements with a range of E_{coh} and G, and use to extrapolate to other elements.

4. Conclusion

The GBDB is, to the best of our knowledge, the most comprehensive database of DFT computed GB energies and work of separation to date, spanning 10 different of GB types, including both tilt and twist GBs, across 58 types of metals. This GBDB has been rigorously validated with previous computational values as well as experimental observations of the GBCD [2,14,15,26,38,60,61]. The linear regression model provides an inexpensive estimate for the GB energy of elemental metals using cohesive energy and shear modulus.

Declaration of Competing Interest

The authors declare that they have no known competing financial interests or personal relationships that could have appeared to influence the work reported in this paper.

Acknowledgement

This work is supported by the Materials Project, funded by the U.S. Department of Energy, Office of Science, Office of Basic Energy Sciences, Materials Sciences and Engineering Division under Contract no. DE-AC02-05-CH11231: Materials Project program KC23MP. The authors also acknowledge computational resources provided by the National Energy Research Scientific Computing Centre (NERSC), the Triton Shared Computing Cluster (TSCC) at the University of California, San Diego, and the Extreme Science and Engineering Discovery Environment (XSEDE) supported by National Science Foundation under grant no. ACI-1053575. The authors thank Professor Gregory S. Rohrer from Carnegie Mellon University for providing the exact values of the experimental GB energies of Ni from Ref [25].

Supplementary material

Supplementary material associated with this article can be found, in the online version, at doi:10.1016/j.actamat.2019.12.030.

References

[1] T. Watanabe, The importance of grain boundary character distribution (GBCD) to recrystallization, grain growth and texture, Scr. Metall. Mater. 27 (11) (1992) 1497–1502, doi:10.1016/0956-716X(92)90134-Z.
[2] G.S. Rohrer, Grain boundary energy anisotropy: a review, J. Mater. Sci. 46 (18) (2011) 5881–5895, doi:10.1007/s10853-011-5677-3.
[3] T. Watanabe, Grain boundary engineering: historical perspective and future prospects, J. Mater. Sci. 46 (12) (2011) 4095–4115, doi:10.1007/s10853-011-5393-z.
[4] C. Hu, J. Huang, B.G. Sumpter, E. Meletis, T. Dumitrică, Ab initio predictions of strong interfaces in transition-metal carbides and nitrides for superhard nanocomposite coating applications, ACS Appl. Nano Mater. 1 (5) (2018) 2029–2035, doi:10.1021/acsanm.8b00227.
[5] T. Watanabe, S. Tsurekawa, The control of brittleness and development of desirable mechanical properties in polycrystalline systems by grain boundary engineering, Acta Mater. 47 (15) (1999) 4171–4185, doi:10.1016/S1359-6454(99)00275-X.

[6] H. Zheng, R. Tran, X.G. Li, B. Radhakrishnan, S.P. Ong, et al., Role of Zr in strengthening MoSi2 from density functional theory calculations, Acta Mater. 145 (2018) 470–476, doi:10.1016/j.actamat.2017.12.017.

[7] E.M. Lehockey, G. Palumbo, On the creep behaviour of grain boundary engineered nickel 1, Mater. Sci. Eng.: A 237 (2) (1997) 168–172, doi:10.1016/S0921-5093(97)00126-3.

[8] P. Shi, R. Hu, T. Zhang, L. Yuan, J. Li, Grain boundary character distribution and its effect on corrosion of Ni–23Cr–16Mo superalloy, Mater. Sci. Technol. 33 (1) (2017) 84–91, doi:10.1179/1743284715Y.0000000142.

[9] S. Kobayashi, T. Inomata, H. Kobayashi, S. Tsurekawa, T. Watanabe, Effects of grain boundary- and triple junction-character on intergranular fatigue crack nucleation in polycrystalline aluminum, J. Mater. Sci. 43 (11) (2008) 3792–3799, doi:10.1007/s10853-007-2236-z.

[10] E.M. Lehockey, G. Palumbo, P. Lin, Improving the weldability and service performance of nickel-and iron-based superalloys by grain boundary engineering, Metall. Mater. Trans. A 29 (12) (1998) 3069–3079, doi:10.1007/s11661-998-0214-y.

[11] G.S. Was, Grain-boundary chemistry and intergranular fracture in austenitic nickel-base alloys: a review, Corrosion 46 (4) (1990) 319–330, doi:10.5006/1.3585110.

[12] U. Krupp, W.M. Kane, X. Liu, O. Dueber, C. Laird, C.J. McMahon, The effect of grain-boundary-engineering-type processing on oxygen-induced cracking of IN718, Mater. Sci. Eng.: A 349 (1) (2003) 213–217, doi:10.1016/S0921-5093(02)00753-0.

[13] A. Pineau, Crossing grain boundaries in metals by slip bands, cleavage and fatigue cracks, Philos. Trans. R. Soc. A: Math. Phys. Eng. Sci. 373 (2038) (2015) 20140131, doi:10.1098/rsta.2014.0131.

[14] G.S. Rohrer, J. Li, S. Lee, A.D. Rollett, M. Groeber, M.D. Uchic, Deriving grain boundary character distributions and relative grain boundary energies from three-dimensional EBSD data, Mater. Sci. Technol. 26 (6) (2010) 661–669, doi:10.1179/026708309X12468927349370.

[15] G.S. Rohrer, E.A. Holm, A.D. Rollett, S.M. Foiles, J. Li, D.L. Olmsted, Comparing calculated and measured grain boundary energies in nickel, Acta Mater. 58 (15) (2010) 5063–5069, doi:10.1016/j.actamat.2010.05.042.

[16] G. Hasson, J.-Y. Boos, I. Herbeuval, M. Biscondi, C. Goux, Theoretical and experimental determinations of grain boundary structures and energies: correlation with various experimental results, Surf. Sci. 31 (1972) 115–137, doi:10.1016/0039-6028(72)90256-7.

[17] K. Barmak, J. Kim, C.-S. Kim, W.E. Archibald, G.S. Rohrer, A.D. Rollett, D. Kinderlehrer, S. Ta'asan, H. Zhang, D.J. Srolovitz, Grain boundary energy and grain growth in Al films: comparison of experiments and simulations, Scr. Mater. 54 (6) (2006) 1059–1063, doi:10.1016/j.scriptamat.2005.11.060.

[18] N.A. Gjostein, F.N. Rhines, Absolute interfacial energies of [001] tilt and twist grain boundaries in copper, Acta Metall. 7 (5) (1959) 319–330, doi:10.1016/0001-6160(59)90198-1.

[19] M. McLean, Grain-boundary energy of copper at 1030C, J. Mater. Sci. 8 (4) (1973) 571–576, doi:10.1007/BF00550462.

[20] S.W. Chan, R.W. Balluffi, Study of energy vs misorientation for grain boundaries in gold by crystallite rotation method-II. Tilt boundaries and mixed boundaries, Acta Metall. 34 (11) (1986) 2191–2199, doi:10.1016/0001-6160(86)90164-1.

[21] H. Miura, M. Kato, T. Mori, Temperature dependence of the energy of Cu [110] symmetrical tilt grain boundaries, J. Mater. Sci. Lett. 13 (1) (1994) 46–48, doi:10.1007/BF02352916.

[22] T. Skidmore, R.G. Buchheit, M.C. Juhas, Grain boundary energy vs. misorientation in Inconel® 600 alloy as measured by thermal groove and OIM analysis correlation, Scr. Mater. 50 (6) (2004) 873–877, doi:10.1016/j.scriptamat.2003.12.004.

[23] G.S. Rohrer, Measuring and interpreting the structure of grain-boundary networks, J. Am. Ceram. Soc. 94 (3) (2011) 633–646, doi:10.1111/j.1551-2916.2011.04384.x.

[24] Y. Amouyal, E. Rabkin, Y. Mishin, Correlation between grain boundary energy and geometry in Ni-rich NiAl, Acta Mater. 53 (14) (2005) 3795–3805, doi:10.1016/j.actamat.2005.04.043.

[25] J. Li, S.J. Dillon, G.S. Rohrer, Relative grain boundary area and energy distributions in nickel, Acta Mater. 57 (14) (2009) 4304–4311, doi:10.1016/j.actamat.2009.06.004.

[26] X. Liu, D. Choi, H. Beladi, N.T. Nuhfer, G.S. Rohrer, K. Barmak, The five-parameter grain boundary character distribution of nanocrystalline tungsten, Scr. Mater. 69 (5) (2013) 413–416, doi:10.1016/j.scriptamat.2013.05.046.

[27] H. Beladi, G.S. Rohrer, The relative grain boundary area and energy distributions in a ferritic steel determined from three-dimensional electron backscatter diffraction maps, Acta Mater. 61 (4) (2013) 1404–1412, doi:10.1016/j.actamat.2012.11.017.

[28] H. Beladi, N.T. Nuhfer, G.S. Rohrer, The five-parameter grain boundary character and energy distributions of a fully austenitic high-manganese steel using three dimensional data, Acta Mater. 70 (2014) 281–289, doi:10.1016/j.actamat.2014.02.038.

[29] M.N. Kelly, K. Glowinski, N.T. Nuhfer, G.S. Rohrer, The five parameter grain boundary character distribution of α-Ti determined from three-dimensional orientation data, Acta Mater. 111 (2016) 22–30, doi:10.1016/j.actamat.2016.03.029.

[30] D. Wolf, Structure-energy correlation for grain boundaries in F.C.C. metals: I. Boundaries on the (111) and (100) planes, Acta Metall. 37 (7) (1989) 1983–1993, doi:10.1016/0001-6160(89)90082-5.

[31] D. Wolf, S. Phillpot, Role of the densest lattice planes in the stability of crystalline interfaces: a computer simulation study, Mater. Sci. Eng.: A A107 (1989) 3–14, doi:10.1016/0921-5093(89)90370-5.

[32] D. Wolf, Correlation between the energy and structure of grain boundaries in b.c.c. metals. II. Symmetrical tilt boundaries, Philos. Mag. A 62 (4) (1990) 447–464, doi:10.1080/01418619008244790.

[33] D. Wolf, A broken-bond model for grain boundaries in face-centered cubic metals, J. Appl. Phys. 68 (7) (1990) 3221–3236, doi:10.1063/1.346373.

[34] D. Wolf, Structure-energy correlation for grain boundaries in F.C.C. metals – III. Symmetrical tilt boundaries, Acta Metall. Mater. 38 (5) (1990) 781–790, doi:10.1016/0956-7151(90)90030-K.

[35] D.L. Olmsted, S.M. Foiles, E.A. Holm, Survey of computed grain boundary properties in face-centered cubic metals: I. Grain boundary energy, Acta Mater. 57 (13) (2009) 3694–3703, doi:10.1016/j.actamat.2009.04.007.

[36] E.A. Holm, D.L. Olmsted, S.M. Foiles, Comparing grain boundary energies in face-centered cubic metals: Al, Au, Cu and Ni, Scr. Mater. 63 (9) (2010) 905–908, doi:10.1016/j.scriptamat.2010.06.040.

[37] M.A. Tschopp, S.P. Coleman, D.L. McDowell, Symmetric and asymmetric tilt grain boundary structure and energy in Cu and Al (and transferability to other fcc metals), Integr. Mater. Manuf. Innov. 4 (1) (2015) 11, doi:10.1186/s40192-015-0040-1.

[38] S. Ratanaphan, D.L. Olmsted, V.V. Bulatov, E.A. Holm, A.D. Rollett, G.S. Rohrer, Grain boundary energies in body-centered cubic metals, Acta Mater. 88 (2015) 346–354, doi:10.1016/j.actamat.2015.01.069.

[39] E.A. Holm, G.S. Rohrer, S.M. Foiles, A.D. Rollett, H.M. Miller, D.L. Olmsted, Validating computed grain boundary energies in fcc metals using the grain boundary character distribution, Acta Mater. 59 (13) (2011) 5250–5256, doi:10.1016/j.actamat.2011.05.001.

[40] D. Scheiber, R. Pippan, P. Puschnig, L. Romaner, Ab initio calculations of grain boundaries in bcc metals, Model. Simul. Mater. Sci. Eng. 24 (3) (2016) 035013, doi:10.1088/0965-0393/24/3/035013.

[41] J. Wang, G.K.H. Madsen, R. Drautz, Grain boundaries in bcc-Fe: a density-functional theory and tight-binding study, Model. Simul. Mater. Sci. Eng. 26 (2) (2018), doi:10.1088/1361-651X/aa9f81.

[42] J.J. Bean, K.P. McKenna, Origin of differences in the excess volume of copper and nickel grain boundaries, Acta Mater. 110 (2016) 246–257, doi:10.1016/j.actamat.2016.02.040.

[43] S.P. Ong, W.D. Richards, A. Jain, G. Hautier, M. Kocher, S. Cholia, D. Gunter, V.L. Chevrier, K.A. Persson, G. Ceder, et al., Python Materials Genomics (pymatgen): A robust, open-source python library for materials analysis, Comput. Mater. Sci. 68 (2013) 314–319, doi:10.1016/j.commatsci.2012.10.028.

[44] S.P. Ong, S. Cholia, A. Jain, M. Brafman, D. Gunter, G. Ceder, K.A. Persson, et al., The materials application programming interface (API): a simple, flexible and efficient API for materials data based on REpresentational State Transfer (REST) principles, Comput. Mater. Sci. 97 (2015) 209–215, doi:10.1016/j.commatsci.2014.10.037.

[45] H. Grimmer, Coincidence-site lattices, Acta Crystallogr. Sect. A 32 (5) (1976) 783–785, doi:10.1107/S056773947601231X.

[46] P. Lejček, Grain boundaries: description, structure and thermodynamics, in: Grain boundary Segregation in Metals, Springer, Berlin, Heidelberg, 2010, pp. 5–24, doi:10.1007/978-3-642-12505-8_2.

[47] J.J. Möller, E. Bitzek, Fracture toughness and bond trapping of grain boundary cracks, Acta Mater. 73 (2014) 1–11, doi:10.1016/j.actamat.2014.03.035.

[48] V.R. Coffman, J.P. Sethna, Grain boundary energies and cohesive strength as a function of geometry, Phys. Rev. B 77 (14) (2008) 144111, doi:10.1103/PhysRevB.77.144111.

[49] M. Grujicic, H. Zhao, G.L. Krasko, Atomistic simulation of 3 (111) grain boundary fracture in tungsten containing various impurities, Int. J. Refract. Metals Hard Mater. 15 (5) (1997) 341–355, doi:10.1016/S0263-4368(97)87508-7.

[50] P. Gumbsch, Atomistic modelling of diffusion-controlled interfacial decohesion, Mater. Sci. Eng.: A 260 (1) (1999) 72–79, doi:10.1016/S0921-5093(98)00984-8.

[51] R. Tran, Z. Xu, B. Radhakrishnan, D. Winston, W. Sun, K.A. Persson, S.P. Ong, et al., Data descripter: surface energies of elemental crystals, Sci. Data 3 (160080) (2016) 1–13, doi:10.1038/sdata.2016.80.

[52] W. Kohn, L.J. Sham, Self-consistent equations including exchange and correlation effects, Phys. Rev. 140 (4A) (1965), doi:10.1103/PhysRev.140.A1133.

[53] G. Kresse, J. Furthmüller, Efficient iterative schemes for ab initio total-energy calculations using a plane-wave basis set, Phys. Rev. B 54 (16) (1996) 11169–11186, doi:10.1103/PhysRevB.54.11169.

[54] P.E. Blöchl, Projector augmented-wave method, Phys. Rev. B 50 (24) (1994) 17953–17979, doi:10.1103/PhysRevB.50.17953.

[55] J.P. Perdew, K. Burke, M. Ernzerhof, Generalized gradient approximation made simple, Phys. Rev. Lett. 77 (18) (1996) 3865–3868, doi:10.1103/PhysRevLett.77.3865.

[56] K. Mathew, J.H. Montoya, A. Faghaninia, S. Dwarakanath, M. Aykol, H. Tang, I.-h. Chu, T. Smidt, B. Bocklund, M. Horton, J. Dagdelen, B. Wood, Z.-k. Liu, J. Neaton, S. Ping, K. Persson, A. Jain, S.P. Ong, K. Persson, A. Jain, S. Ping, K. Persson, A. Jain, Atomate: a high-level interface to generate, execute, and analyze computational materials science workflows, Comput. Mater. Sci. 139 (2017) 140–152, doi:10.1016/j.commatsci.2017.07.030.

[57] A. Jain, S.P. Ong, W. Chen, B. Medasani, X. Qu, M. Kocher, M. Brafman, G. Petretto, G.-M. Rignanese, G. Hautier, D. Gunter, K.A. Persson, et al., FireWorks: a dynamic workflow system designed for high-throughput

applications, Concurr. Comput.: Pract. Exp. 27 (17) (2015) 5037–5059, doi:10.1002/cpe.3505.
[58] N. Gaston, D. Andrae, B. Paulus, U. Wedig, M. Jansen, et al., Understanding the hcp anisotropy in Cd and Zn: the role of electron correlation in determining the potential energy surface, Phys. Chem. Chem. Phys. 12 (3) (2010) 681–687, doi:10.1039/B915967C.
[59] D. Wolf, Structure and energy of general grain boundaries in bcc metals, J. Appl. Phys. 69 (1) (1991) 185–196, doi:10.1063/1.347741.
[60] D.M. Saylor, B.S. El Dasher, A.D. Rollett, G.S. Rohrer, Distribution of grain boundaries in aluminum as a function of five macroscopic parameters, Acta Mater. 52 (12) (2004) 3649–3655, doi:10.1016/j.actamat.2004.04.018.
[61] H. Beladi, G.S. Rohrer, The distribution of grain boundary planes in interstitial free steel, Metall. Mater. Trans. A 44 (1) (2013) 115–124, doi:10.1007/s11661-012-1393-0.
[62] S.K. Bhattacharya, S. Tanaka, Y. Shiihara, M. Kohyama, et al., Ab initio study of symmetrical tilt grain boundaries in bcc Fe: structural units, magnetic moments, interfacial bonding, local energy and local stress, J. Phys. Condens. Matter 25 (13) (2013), doi:10.1088/0953-8984/25/13/135004.
[63] E. Wachowicz, T. Ossowski, A. Kiejna, Cohesive and magnetic properties of grain boundaries in bcc Fe with Cr additions, Phys. Rev. B 81 (9) (2010) 94104, doi:10.1103/PhysRevB.81.094104.
[64] N. Gao, C.C. Fu, M. Samaras, R. Schäublin, M. Victoria, W. Hoffelner, Multiscale modelling of bi-crystal grain boundaries in bcc iron, J. Nucl. Mater. 385 (2) (2009) 262–267, doi:10.1016/j.jnucmat.2008.12.016.
[65] Y.A. Du, L. Ismer, R. Jutta, T. Hickel, J. Neugebauer, R. Drautz, First-principles study on the interaction of H interstitials with grain boundaries in α and γ-Fe, Phys. Rev. B 84 (14) (2011) 144121, doi:10.1103/PhysRevB.84.144121.
[66] M. čák, M. Šob, J. Hafner, First-principles study of magnetism at grain boundaries in iron and nickel, Phys. Rev. B – Condens. Matter Mater. Phys. 78 (5) (2008) 1–10, doi:10.1103/PhysRevB.78.054418.
[67] T. Ochs, O. Beck, C. Elsässer, B. Meyer, Symmetrical tilt grain boundaries in body-centred cubic transition metals: an ab initio local-density-functional study, Philos. Mag. A 80 (2) (2000) 351–372, doi:10.1080/01418610008212057.
[68] A.F. Wright, S.R. Atlas, Density-functional calculations for grain boundaries in aluminum, Phys. Rev. B 50 (20) (1994) 15248–15260, doi:10.1103/PhysRevB.50.15248.
[69] S. Ogata, H. Kitagawa, Y. Maegawa, K. Saitoh, Ab-initio analysis of aluminum $\Sigma = 5$ grain boundaries fundamental structures and effects of silicon impurity, Comput. Mater. Sci. 7 (3) (1997) 271–278, doi:10.1016/S0927-0256(96)00095-X.
[70] V.I. Razumovskiy, A.V. Ruban, I.M. Razumovskii, A.Y. Lozovoi, V.N. Butrim, Y.K. Vekilov, The effect of alloying elements on grain boundary and bulk cohesion in aluminum alloys: An ab initio study, Scr. Mater. 65 (10) (2011) 926–929, doi:10.1016/j.scriptamat.2011.08.014.
[71] S. Zhang, O.Y. Kontsevoi, A.J. Freeman, G.B. Olson, Sodium-induced embrittlement of an aluminum grain boundary, Phys. Rev. B 82 (22) (2010) 224107, doi:10.1103/PhysRevB.82.224107.
[72] G. Lu, N. Kioussis, Interaction of vacancies with a grain boundary in aluminum: a first-principles study, Phys. Rev. B – Condens. Matter Mater. Phys. 64 (2) (2001) 1–7, doi:10.1103/PhysRevB.64.024101.
[73] V.I. Razumovskiy, I.M. Razumovskii, A.V. Ruban, V.N. Butrim, Y. Vekilov, The influence of alloying elements on grain boundary and bulk cohesion in aluminum alloys: ab initio study, Adv. Mater. Res. THERMEC 2011 Supplement 409 (2011) 417–422. https://www.scientific.net/AMR.409.417.
[74] T. Ossowski, E. Wachowicz, A. Kiejna, Effect of iron additions on intergranular cohesion in chromium, J. Phys.: Condens. Matter 21 (48) (2009) 485002, doi:10.1088/0953-8984/21/48/485002.
[75] J. Xu, J.-B. B. Liu, S.-N. N. Li, B.-X. X. Liu, Y. Jiang, Self-healing properties of nanocrystalline materials: a first-principles analysis of the role of grain boundaries, Phys. Chem. Chem. Phys. 18 (27) (2016) 17930–17940, doi:10.1039/C6CP02505F.
[76] G. Schusteritsch, T.D. Kühne, Z.X. Guo, E. Kaxiras, The effect of Ag, Pb and Bi impurities on grain boundary sliding and intergranular decohesion in Copper, Philos. Mag. 96 (27) (2016) 2868–2886, doi:10.1080/14786435.2016.1217360.
[77] A.Y. Lozovoi, A.T. Paxton, M.W. Finnis, Structural and chemical embrittlement of grain boundaries by impurities: a general theory and first-principles calculations for copper, Phys. Rev. B 74 (15) (2006) 155416, doi:10.1103/PhysRevB.74.155416.
[78] Y. Cui, H.B. Chew, A simple numerical approach for reconstructing the atomic stresses at grain boundaries from quantum-mechanical calculations, J. Chem. Phys. 150 (14) (2019) 144702, doi:10.1063/1.5085061.
[79] Z. Huang, F. Chen, Q. Shen, L. Zhang, T.J. Rupert, Uncovering the influence of common nonmetallic impurities on the stability and strength of a $\Sigma5$ (310) grain boundary in Cu, Acta Mater. 148 (2018) 110–122, doi:10.1016/j.actamat.2018.01.058.
[80] M. Yamaguchi, M. Shiga, H. Kaburaki, Grain boundary decohesion by sulfur segregation in ferromagnetic iron and nickel – a first-principles study, Mater. Trans. 47 (11) (2006) 2682–2689, doi:10.2320/matertrans.47.2682.
[81] M. Yamaguchi, First-principles study on the grain boundary embrittlement of metals by solute segregation: Part I. Iron (Fe)-solute (B, C, P, and S) systems, Metall. Mater. Trans. A 42 (2) (2011) 319–329, doi:10.1007/s11661-010-0381-5.
[82] Z. Xu, S. Tanaka, M. Kohyama, Grain-boundary segregation of 3d-transition metal solutes in bcc Fe: ab initio local-energy and d-electron behavior analysis, J. Phys.: Condens. Matter 31 (11) (2019) 115001, doi:10.1088/1361-648x/aafd00.
[83] K.-D.D. Bauer, M. Todorova, K. Hingerl, J. Neugebauer, A first principles investigation of zinc induced embrittlement at grain boundaries in bcc iron, Acta Mater. 90 (2015) 69–76, doi:10.1016/j.actamat.2015.02.018.
[84] A.M. Tahir, R. Janisch, A. Hartmaier, Ab initio calculation of traction separation laws for a grain boundary in molybdenum with segregated C impurites, Modell. Simul. Mater. Sci. Eng. 21 (7) (2013) 075005, doi:10.1088/0965-0393/21/7/075005.
[85] R. Janisch, C. Elsässer, Growth and mechanical properties of a MoC precipitate at a Mo grain boundary: an ab initio density functional theory study, Phys. Rev. B 77 (9) (2008) 94118, doi:10.1103/PhysRevB.77.094118.
[86] R. Tran, Z. Xu, N. Zhou, B. Radhakrishnan, J. Luo, S.P. Ong, et al., Computational study of metallic dopant segregation and embrittlement at molybdenum grain boundaries, Acta Materialia 117 (2016) 91–99, doi:10.1016/j.actamat.2016.07.005.
[87] M. Yamaguchi, M. Shiga, H. Kaburaki, Energetics of segregation and embrittling potency for non-transition elements in the Ni $\Sigma5$ (012) symmetrical tilt grain boundary: a first-principles study, J. Phys.: Condens. Matter 16 (23) (2004) 3933–3956, doi:10.1088/0953-8984/16/23/013.
[88] V.I. Razumovskiy, A.Y. Lozovoi, I.M. Razumovskii, First-principles-aided design of a new Ni-base superalloy: Influence of transition metal alloying elements on grain boundary and bulk cohesion, Acta Mater. 82 (2015) 369–377, doi:10.1016/j.actamat.2014.08.047.
[89] E.L.T. Bentria, I.K. Lefkaier, B. Bentria, The effect of vanadium impurity on Nickel Sigma 5(012) grain boundary, Mater. Sci. Eng. A 577 (2013) 197–201, doi:10.1016/j.msea.2013.04.047.
[90] Y. Zhang, W.-Q. Feng, Y.-L. Liu, G.-H. Lu, T. Wang, First-principles study of helium effect in a ferromagnetic iron grain boundary: energetics, site preference and segregation, Nucl. Instrum. Methods Phys. Res. Sect. B: Beam Interact. Mater. Atoms 267 (18) (2009) 3200–3203, doi:10.1016/j.nimb.2009.06.064.
[91] M. Všianská, M. Šob, The effect of segregated sp-impurities on grain-boundary and surface structure, magnetism and embrittlement in nickel, Progr. Mater. Sci. 56 (6) (2011) 817–840, doi:10.1016/j.pmatsci.2011.01.008.
[92] L. Chen, P. Peng, H.-L. Zhuang, D.-W. Zhou, First-principle investigation of bismuth segregation at $\Sigma5$ (012) grain-boundaries in nickel, Trans. Nonferrous Metals Soc. China 16 (10) (2006) s813–s819, doi:10.1016/S1003-6326(06)60306-3.
[93] X. Wu, X.S. Kong, Y.W. You, W. Liu, C.S. Liu, J.L. Chen, G.N. Luo, Effect of transition metal impurities on the strength of grain boundaries in vanadium, J. Appl. Phys. 120 (9) (2016) 95901, doi:10.1063/1.4961867.
[94] W. Setyawan, R.J. Kurtz, Ab initio study of H, He, Li and Be impurity effect in tungsten $\Sigma3\{112\}$ and $\Sigma27$ {552} grain boundaries, J. Phys.: Condens. Matter 26 (13) (2014) 135004, doi:10.1088/0953-8984/26/13/135004.
[95] D. Scheiber, V.I. Razumovskiy, P. Puschnig, R. Pippan, L. Romaner, Ab initio description of segregation and cohesion of grain boundaries in W-25at.% Re alloys, Acta Mater. 88 (2015) 180–189, doi:10.1016/j.actamat.2014.12.053.
[96] X. Wu, Y.-W. W. You, X.-S. S. Kong, J.-L. L. Chen, G.-N. N. Luo, G.-H. H. Lu, C.S. Liu, Z. Wang, First-principles determination of grain boundary strengthening in tungsten: Dependence on grain boundary structure and metallic radius of solute, Acta Mater. 120 (2016) 315–326, doi:10.1016/j.actamat.2016.08.048.
[97] M. Christensen, T.M. Angeliu, J.D. Ballard, J. Vollmer, R. Najafabadi, E. Wimmer, Effect of impurity and alloying elements on Zr grain boundary strength from first-principles computations, J. Nucl. Mater. 404 (2) (2010) 121–127, doi:10.1016/j.jnucmat.2010.07.012.
[98] S. Plimpton, Fast parallel algorithms for short-range molecular dynamics, J. Comput. Phys. 117 (1) (1995) 1–19, doi:10.1006/jcph.1995.1039.
[99] C. Chen, Z. Deng, R. Tran, H. Tang, I.-h. Chu, S.P. Ong, et al., Accurate force field for molybdenum by machine learning large materials data, Phys. Rev. Mater. 1 (4) (2017) 043603, doi:10.1103/PhysRevMaterials.1.043603.
[100] X.-G. Li, C. Hu, C. Chen, Z. Deng, J. Luo, S.P. Ong, Quantum-accurate spectral neighbor analysis potential models for Ni–Mo binary alloys and fcc metals, Phys. Rev. B 98 (9) (2018) 94104, doi:10.1103/PhysRevB.98.094104.
[101] W.T. Geng, A.J. Freeman, R. Wu, G.B. Olson, Effect of Mo and Pd on the grain-boundary cohesion of Fe, Phys. Rev. B 62 (10) (2000) 6208–6214, doi:10.1103/PhysRevB.62.6208.
[102] Y.Q. Fen, C.Y. Wang, Electronic effects of nitrogen and phosphorus on iron grain boundary cohesion, Comput. Mater. Sci. 20 (1) (2001) 48–56, doi:10.1016/S0927-0256(00)00124-5.
[103] J.S. Braithwaite, P. Rez, Grain boundary impurities in iron, Acta Mater. 53 (9) (2005) 2715–2726, doi:10.1016/j.actamat.2005.02.033.
[104] H. Jin, I. Elfimov, M. Militzer, Study of the interaction of solutes with $\Sigma5$ (013) tilt grain boundaries in iron using density-functional theory, J. Appl. Phys. 115 (9) (2014) 093506, doi:10.1063/1.4867400.
[105] E.J. McEniry, T. Hickel, J. Neugebauer, Hydrogen behaviour at twist {110} grain boundaries in α-Fe, Philos. Trans. R. Soc. A: Math. Phys. Eng. Sci. 375 (2098) (2017), doi:10.1098/rsta.2016.0402.
[106] A.Y. Lozovoi, A.T. Paxton, Boron in copper: a perfect misfit in the bulk and cohesion enhancer at a grain boundary, Phys. Rev. B 77 (16) (2008) 165413, doi:10.1103/PhysRevB.77.165413.
[107] F. Meng, X. Lu, Y. Liu, Y. Qi, First-principles study on the effect and magnetism of iron segregation in Cu grain boundary, J. Mater. Sci. 52 (8) (2017) 4309–4322, doi:10.1007/s10853-016-0526-z.
[108] V.I. Razumovskiy, S.V. Divinski, L. Romaner, Solute segregation in Cu: DFT vs. Experiment, Acta Mater. 147 (2018) 122–132, doi:10.1016/j.actamat.2018.01.011.

[109] D. Scheiber, R. Pippan, P. Puschnig, L. Romaner, Ab initio search for cohesion-enhancing impurity elements at grain boundaries in molybdenum and tungsten, Model. Simul. Mater. Sci. Eng. 24 (8) (2016) 85009, doi:10.1088/0965-0393/24/8/085009.
[110] Y.-J. Hu, G. Zhao, B. Zhang, C. Yang, M. Zhang, Z.-K. Liu, X. Qian, L. Qi, Local electronic descriptors for solute-defect interactions in bcc refractory metals, Nat. Commun. 10 (1) (2019) 4484, doi:10.1038/s41467-019-12452-7.
[111] matweb, Material property data, 2019, Last accessed 14 April 2019, http://www.matweb.com/.
[112] R. Hill, The elastic behaviour of a crystalline aggregate, Proc. Phys. Soc. Sect. A 65 (5) (1952) 349–354, doi:10.1088/0370-1298/65/5/307.
[113] M. de Jong, W. Chen, T. Angsten, A. Jain, R. Notestine, A. Gamst, M. Sluiter, C. Krishna Ande, S. van der Zwaag, J.J. Plata, C. Toher, S. Curtarolo, G. Ceder, K.A. Persson, M. Asta, et al., Charting the complete elastic properties of inorganic crystalline compounds, Sci. Data 2 (2015) 150009, doi:10.1038/sdata.2015.9.
[114] W.T. Read, W. Shockley, V. Number, Dislocation models of crystal grain boundaries, Phys. Rev. 78 (3) (1950) 275–289, doi:10.1103/PhysRev.78.275.